2020

Solvothermal synthesis of copper-doped BiOBr microflowers with enhanced adsorption and visible-light driven photocatalytic degradation of norfloxacin

Xincong Lv

Dickson Y.S. Tan

Frank Leung Yuk Lam

Yun Hau Ng

Shengming Yin

See next page for additional authors

Thei

Member of VTC Group
VTC 機構成員

Authors

Xincong Lv, Dickson Y.S. Tan, Frank Leung Yuk Lam, Yun Hau Ng, Shengming Yin, and Alicia Kyoingjin An

Solvothermal synthesis of copper-doped BiOBr microflowers with enhanced adsorption and visible-light driven photocatalytic degradation of norfloxacin

Xincong Lv[a,b], Dickson Y.S. Yan[c], Frank Leung-Yuk Lam[d,*], Yun Hau Ng[a], Shengming Yin[a], Alicia Kyoungjin An[a,*]

[a] School of Energy and Environment, City University of Hong Kong, Tat Chee Avenue Kowloon, Hong Kong, China
[b] International Collaborative Laboratory of 2D Materials for Optoelectronics Science and Technology of Ministry of Education, Institute of Microscale Optoelectronics, Shenzhen University, Shenzhen 518060, China
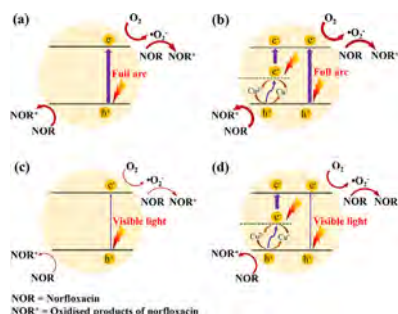[c] Faculty of Science & Technology, The Technological and Higher Education Institute of Hong Kong, 20A, Tsing Yi Road, New Territories, Hong Kong, China
[d] Department of Chemical and Biological Engineering, The Hong Kong University of Science and Technology, Clear Water Bay, Kowloon, Hong Kong, China

HIGHLIGHTS

- Copper doped BiOBr (Cu-doped BiOBr) was synthesized using a one-step hydrothermal method.
- Cu-doped BiOBr showed much higher visible-light-driven photocatalytic activity for norfloxacin degradation.
- The doping of copper in BiOBr enhance the norfloxacin adsorption on photocatalyst surface.
- The photocatalytic activity of Cu-doped BiOBr in the fifth cycle easily maintained 95% of the activity in the first cycle.

GRAPHICAL ABSTRACT

NOR = Norfloxacin
NOR* = Oxidised products of norfloxacin

ABSTRACT

Photocatalysts based on copper-doped bismuth oxybromide (Cu-doped BiOBr) were synthesised using a solvothermal method and assessed for their ability to degrade norfloxacin under visible light. The Cu atoms were successfully doped into the crystal lattice of BiOBr, yielding Cu-doped BiOBr microflowers with a morphology and crystal structure identical to that of pristine BiOBr. The as-prepared Cu-doped BiOBr showed activity superior to BiOBr in the photocatalytic degradation of norfloxacin under visible-light irradiation, which was attributed to its improved light-harvesting properties, enhanced charge separation and interfacial charge transfer. Furthermore, we found for the first time that the introduction of Cu into BiOBr enhanced the adsorption capacity between the photocatalyst and norfloxacin, which we considered to be the main contribution to its improved performance. Cu-doped BiOBr containing the optimal proportion of Cu and Bi (Cu:Bi = 0.03) had a photocatalytic degradation constant of 0.64×10^{-2} min^{-1}, which is 2.28 times higher than that of undoped BiOBr. The primary oxidation pathway was determined to involve the transfer of photogenerated holes to norfloxacin. Finally, we demonstrated that the Cu-doped BiOBr photocatalyst retained 95% of its initial activity even after five successive catalytic cycles, confirming its recyclability.

1. Introduction

Norfloxacin (NOR) is a member of the fluoroquinolone class of antibiotics, and has been widely used in both humans and animals [1]. However, as NOR cannot be fully metabolised in the body, most of it is excreted and enters the environment via wastewater effluents. Previous studies verified that NOR is toxic to plants [2] and aquatic organisms [3], and that it may also induce irreversible adverse effects and threaten ecosystems by increasing bacterial resistance to drugs [3] and spreading the genes for antibiotic resistance in bacterial populations. Thus, it is vital to remove NOR from wastewater before it is discharged into the environment.

A number of techniques have been proposed for removing NOR from wastewater, including adsorption [4], electrochemical oxidation [5], advanced oxidation processes (AOPs) [6]. Methods based on adsorption processes, such as biosorption onto microbial biomass [7], adsorption on carbon nanotubes [8], or in magnetic molecular imprinted chitosan/γ-Fe$_2$O$_3$ [9] has been tested. However, the "removed" NOR only physically resides in the sorbent and creates a risk of being released into the aquatic environment if the used sorbent is improperly disposed. Although the electrochemical oxidation of NOR has been promoted as a promising alternative technique [5,10], the requirement of electricity will inevitably raise the treatment cost. AOPs are seen as environmentally friendly technologies, since their reactions with inorganic and organic compounds can generate CO_2, H_2O, and inorganic compounds in the case of full mineralization. Different types of AOPs, including chemical oxidation (O_3, Fenton reagents), photochemical oxidation (UV/O_3, UV/H_2O_2) and heterogeneous photocatalysis (UV/TiO$_2$), have received significant attention for the treatment of wastewater due to the generation of highly reactive species, namely hydroxyl radicals ($\cdot OH^-$) [11,12]. Recently, AOPs based on the sulfate radical ($SO_4 \cdot ^-$) were also found to be promising technologies due to their longer half-life and broader pH range compared with $\cdot OH^-$ [13–15]. The combination of photocatalysis and chemical oxidation processes has been reported by Boczkaj and their co-workers, who constructed the TiO$_2$/UV/O$_3$/H$_2$O$_2$ system for the treatment of wastewater at lower process costs [16,17].

Photocatalysis is one of the most studied and economically feasible AOPs due to only requiring light energy and operating under mild temperature and pressure conditions without the need for additional chemicals. Up to now, the most widely studied semiconductor photocatalysts for degradation of pharmaceutical compounds focused on TiO$_2$ and ZnO, including C-TiO$_2$ [18], Ag$_2$O/TiO$_2$-zeolite composite [19], Bi^{3+} and Fe^{2+} co-doped ZnO [20], ZnO/nano-cellulose composites [21] and powdered stone waste supported ZnO [22]. However, the large bandgap of them limits their visible light photo-absorptivity and hinders exploitation of their energetic potential [23,24]. Among the group of V–VI–VII semiconductors, bismuth oxyhalides are of great importance because of their optical properties and promising industrial applications, such as in photocatalysis, ferroelectric materials and pigments [25–27]. BiOBr, which is crystalline and composed of $[Bi_2O_2]^{2+}$ layers interleaved with double Br layers, has attracted considerable attention because of its suitable bandgap, stability and superior visible-light-induced photocatalytic activity [28,29]. Despite these advantages, its overall photocatalytic efficiency is still comparatively low due to its relatively large electronic bandgap ($E_g = 2.90$ eV) [30] and the rapid recombination of photo-induced electron-hole pairs [28,31]. Modification of BiOBr is necessary to improve the harvesting of solar energy and facilitate efficient utilizing of photo-induced charges.

Incorporation of main group elements (especially metal and non-metal ions) into BiOBr lattices has gained much attention due to these elements' ability to modify the surface electronic properties and thus enhance the photocatalytic activity. The redox energy states of transition metal ions (e.g. Cu, Co, Ni, Cr, Mn, Fe) mostly lie within the band gap states of BiOBr. This introduces an intra-band state close to the conduction band (CB) or valence band (VB) edge, which induces visible light absorption at sub-band gap energies. Chen and his co-workers prepared the Fe-doped BiOBr with enhanced photocatalytic activity and observe the redox energy states of Fe by the cyclic voltammetry measurement [32]. Non-metal doping (e.g. N, S, B, I) will elevate the valence band, which can narrow the band gap of BiOBr. For example, the doping of I$^-$ ions significantly enhanced the activity of BiOBr owing to the elevated VB potential [33]. Boron, a non-metal, was doped into BiOBr, and the resulting material exhibited enhanced photocatalytic inactivation of *Escherichia coli* compared to non-doped BiOBr. This was attributed to improved charge-carrier separation efficiency, arising from the ability of the B dopants level to accept extra electrons from the VB of BiOBr [34]. Copper is a photoactive transition metal, thus its presence in a semiconductor photocatalyst may modify the electronic and photophysical properties of the overall material. Guo and Du reported that Cu doping can broaden the adsorption edge of TiO$_2$ in the visible region by forming dopant states above the VB caused by the Cu 3d orbital [35]. The formation of Cu dopant electronic states in the midgap was also discovery in ZnO [36], SnO$_2$ [37] and Bi$_2$O$_3$ [38]. The doping of Cu into BiOBr has also been reported to enhance photocatalytic activity due to narrow the band gap of BiOBr [39,40].

It is well known that adsorption of organics or antibiotics on photocatalysts is a prerequisite for highly efficient utilizing photo-induced electron-hole pairs due to the low diffusion of the charge carriers into the solution [41,42]. The organics or antibiotics first can be enriched from a large amount of wastewater and then be removed by photocatalytic degradation process, and the adsorption ability of the material is recovered at the same time. Most of work on improving the adsorption abilities of BiOBr were performed by adjusting the morphologies, reducing the crystal size and incorporating with other high-surface-area materials [43,44]. Nevertheless, few people pay attention to the adsorption capacity of ions doped BiOBr.

In present work, we synthesised Cu-doped BiOBr microflowers via a simple solvothermal route and systemically investigated the photocatalytic degradation of NOR over this material. Cu-doped BiOBr exhibited more efficient visible-light-driven photocatalytic activity than that of pristine BiOBr, which led to enhanced light harvesting into illumination with longer wavelength and a more effective transfer of the photogenerated carriers. Importantly, the presence of the Cu element would enhance the adsorption affinity likely through interacting with the exposed functional groups of the N–H and COO– of the norfloxacin molecules, which then greatly increases the reaction rate of the heterogeneous catalysis and its rapid photocatalytic degradation of NOR. To the best of our knowledge, this paper is the first to report the integration of adsorption abilities and light harvesting through the doping with foreign ions into BiOBr.

2. Experimental section

2.1. Preparation and characterisation of photocatalyst

The Cu-doped BiOBr samples were prepared by a solvothermal method, as described below. 5 mM potassium bromide (99%, Aldrich), 5 mM bismuth nitrate pentahydrate (Bi(NO$_3$)$_3$·5H$_2$O, 98%, Aldrich) and different amount (0.05 ~ 0.25 mM) of copper (II) nitrate hemi(pentahydrate) (Cu(NO$_3$)$_2$·2.5H$_2$O, 98%, Aldrich) were added to 100 mL ethylene glycol (99.8%, Aldrich). The mixture was stirred for 60 min and the resulting homogenous mixture was transferred into a 150 mL Teflon-lined stainless-steel autoclave and then heated at 160 °C for 12 h. Subsequently, the autoclave was gradually cooled to room temperature. The resulting precipitate was rinsed successively with 40 mL deionised water (18.2 MΩ, Millipore) (×3) and 40 mL ethanol (×3) to remove any impurities. The resulting Cu-doped BiOBr was dried in a vacuum oven at 80 °C for 8 h. Pure BiOBr was also prepared under the same conditions (i.e., without the addition of Cu(NO$_3$)$_2$·2.5H$_2$O).

The morphologies of the Cu-doped BiOBr samples were characterised using scanning electron microscope (SEM, MIRA3, TESCAN)

and transmission electron microscopy (TEM; JEM-2100) operating at 200 kV. X-ray diffraction (XRD) was performed on a Philips X'Pert PRO with Cu-Kα at 40 kV and 40 mA as the radiation source. Diffraction patterns were collected in the 2θ range of 10–90° with a step size of 0.01°. The surface composition of the samples was analysed by X-ray photoelectron spectroscopy (XPS; Physical Electronics PHI 5802) using Al-Kα as the radiation source.

Peak deconvolution and spectral analysis were conducted using XPS Peak software with binding energies referenced to that of C 1s at 284.6 eV. The chemical constituents of as-prepared samples were measured by X-ray fluorescence (XRF) spectrometer (PANalytical Axios). The diffuse reflectance spectra were measured on a UV–Vis spectrophotometer (Shimadzu 2600) equipped with a BaSO$_4$ integrating sphere. The obtained reflectance spectra were converted to absorption spectra using the Kubelka-Munk function, $F(R) = (1 - R)^2/2R$, where R is the measured reflectance.

Thermogravimetric (TG) analysis was conducted in a thermal analyser (SDT-Q500, TA Instruments) in air from 25 °C to 800 °C at a rate of 5 °C/min. Zeta potential analysis was performed using a Malvern Nano-ZS. N$_2$ adsorption–desorption experiments at 77 K were carried out using a Micromeritics 3-Flex. All samples were degassed at 383 K overnight under vacuum prior to measurements being made, and the surface areas were obtained from the BET model. Adsorption isotherms were measured with 1.0 mg mL^{-1} photocatalyst suspension in the presence of different concentrations of NOR. After 24 h of continuous stirring in the dark, a suspension was filtered and an aliquot was analysed by UV–vis spectrophotometry (Shimadzu 2600) at a wavelength of 276 nm. The metal leaching (i.e. Cu^{2+} and Bi^{3+}) from the photocatalyst was measured by inductively coupled plasma mass spectrometry (ICP-MS, Varian820-MS)". The turnover frequencies (TOFs) were calculated from the initial degradation rates of the NOR, and normalized to the number of surface active sites estimated from the saturated adsorption molecule number (*N*) of NOR on different photocatalysts.

The photocatalyst was characterised before and after NOR adsorption by FTIR spectroscopy (Shimadzu IRAffinity-1) to determine the mode of adsorption. Photoelectrochemical (PEC) characterisation was carried out using a CH Instrument 660D station. A standard three-electrode system consisting of the photoelectrode as the working electrode, an Ag/AgCl reference electrode and a platinum (Pt) counter-electrode was set up in a customised Teflon cell fitted with a quartz irradiation window. For the preparation of the photoelectrodes, a solution of BiOBr or Cu-doped BiOBr in ethanol (absolute, Aldrich) was sonicated and drop-cast onto pre-cut fluorine-doped tin oxide conductive glass (1 cm × 5 cm, FTO, Nippon Sheet Glass) to yield dry photocatalyst at a loading of 1 mg cm^{-2}. Prior to the PEC measurements, the 0.2 M Na$_2$SO$_4$ (≥99.0%, Aldrich) aqueous electrolyte was deaerated by N$_2$ purging for 30 min. Photocurrent measurements were conducted at potential of 1 V versus the RHE (pH 0), using a light shield every 10 s. Irradiation was provided by a 200 W Hg (Xe) arc lamp (Newport) with or without a 420 nm long-pass filter (Oriel, CGA420).

2.2. DFT calculation

Density functional theory (DFT) calculations were performed by employing the Vienna Ab initio Simulation Package (VASP) [45]. The energy cutoff for the projector-augmented wave pseudopotentials [46] was 400 eV. A (4 × 4 × 2) and a tetragonal supercell containing 64 formula units of BiOBr (192 atoms) was used to study point defects. We obtained the defective Cu-BiOBr structure by replacing a Br atom in the BiOBr supercell with a Cu atom. The Perdew–Burke–Ernzerhof (PBE) exchange–correlation functional [47] was applied to obtain the bulk BiOBr structure. Meanwhile, we used a PBE + U approach to optimize the Cu-BiOBr structure with a Coulomb parameter of U = 5.0 eV for the d-orbitals of the Cu atoms [48]. We applied spin-unpolarized calculations, as there is no unpaired electron in the two systems. The two structures were allowed to fully optimize until the ion force was less

than 0.02 eV/Å. Due to the large supercell, the Γ-point sampling was used in the calculations. Fig. S1 shows the optimized structures of the pristine BiOBr and defective Cu-BiOBr supercells.

2.3. Photocatalytic degradation experiments

Photocatalytic assessments were carried out in a customised Pyrex glass photoreactor equipped with a cooling-water jacket (2 cm) as shown in Scheme S1. A photocatalyst suspension (1.0 mg mL^{-1}, 150 mL) containing 10 ppm of dissolved NOR (98%, Dieckmann) was allowed to adsorb for 45 min in the dark with magnetic stirring at 600 rpm. The adsorption experiment results confirm that 45 min is enough to approach equilibrium (Fig. S2). The turbidity of different concentrations of photocatalyst (0.67, 1, 1.4 and 2 mg/mL) were measured to be 901, 1154, 1880 and 2976 NTU by the turbidimeter (HACH 2100Q Portable Turbidimeter). Irradiation was provided by a 200 W Hg (Xe) arc lamp with no filtering (full arc, 190 mW cm^{-2}), or with a 420 nm cut-off filter (visible light, 100 mW cm^{-2}) placed in front of the lamp. During the reusability tests, the photocatalysts were recovered by centrifuging the treated solution at 8000 rpm/min and then sinter it at 250 °C to remove the surface organics. At certain time intervals, 3 mL aliquots of the suspension were removed and passed through a 0.45 μm nylon membrane to filter off photocatalyst particles. The concentration of NOR in the resulting filtrate was determined by UV–vis spectrophotometry (Shimadzu 2600) at a wavelength of 276 nm. The leached components of the catalysts during the experiments have no absorption at 276 nm (Fig. S3).

The intermediates were analysed by UPLC-MS system consisted of a Waters ACQUITY® UPLC® (Waters Corporation, Milford, MA, USA) coupled to a Triple TOF 4600 mass spectrometer with a DuoSprayTM source operating in the positive ESI mode was used for detection (AB SCIEX, CA, USA). Chromatographic separations were carried out using the Acquity UPLC BEH (bridged ethyl hybrid) C18 column; 2.1 × 100 mm, and 1.7 μm particle size. The column was maintained at 40 °C. The following gradient was used: 0 min, 95% of eluent A and 5% of eluent B; 10 min, 0% of eluent A and 100% of eluent B, at a flow rate of 0.3 mL min^{-1}. Eluent A: 0.1%(v/v) formic acid in water; eluent B: 0.1% (v/v) formic acid in acetonitrile. Chromatograms were recorded using Waters eλ PDA detector. MS detection settings were as follows: ion spray voltage, 5.5 kV; ion source heater, 450 °C; curtain gas, 30 psi; ion source gas 1, 40 psi; and ion source gas 2, 40 psi. and a 250-ms accumulation time for the Full MS and a 100-ms accumulation time for the MS/MS experiments.

3. Results and discussion

3.1. Physicochemical characterisation of Cu-doped BiOBr

The morphologies of the samples were examined by SEM and TEM, as shown in Fig. 1. The low-magnification SEM images (Fig. 1a) suggest that the BiOBr microflowers have been obtained on a large scale after solvothermal treatment at 160 °C for 12 h, which agrees with the result's reported by Qiu [49]. The introduction of copper ions did not change the morphologies as shown in Fig. 1d. Moreover, the elemental mapping images (displayed in Fig. S4, supporting information) demonstrate the uniform distribution of Cu, in the BiOBr hierarchical microflowers. The EDS spectrum of pure BiOBr (Fig. S5a) shows the presence of Bi, O and Br elements whereas the Cu-BiOBr (Fig. S5b) shows the presence of Cu in addition to Bi, O, and Br, elements. It was found that the ratio of Bi to Br (1.03) is very close to the stoichiometric ratio (Table S1), indicating the formation of BiOBr. The ratio increases to 1.47 in the 3%Cu-BiOBr, which suggests that the Cu occupies the Br position. To obtain the accurate chemical composition in bulk samples, BiOBr and 3%Cu-BiOBr were characterized by XRF as shown in Fig. S6. The ratio of Bi to Br in BiOBr (1.07) is in agreement with the input (1.00), which has also been reported by other researchers using the
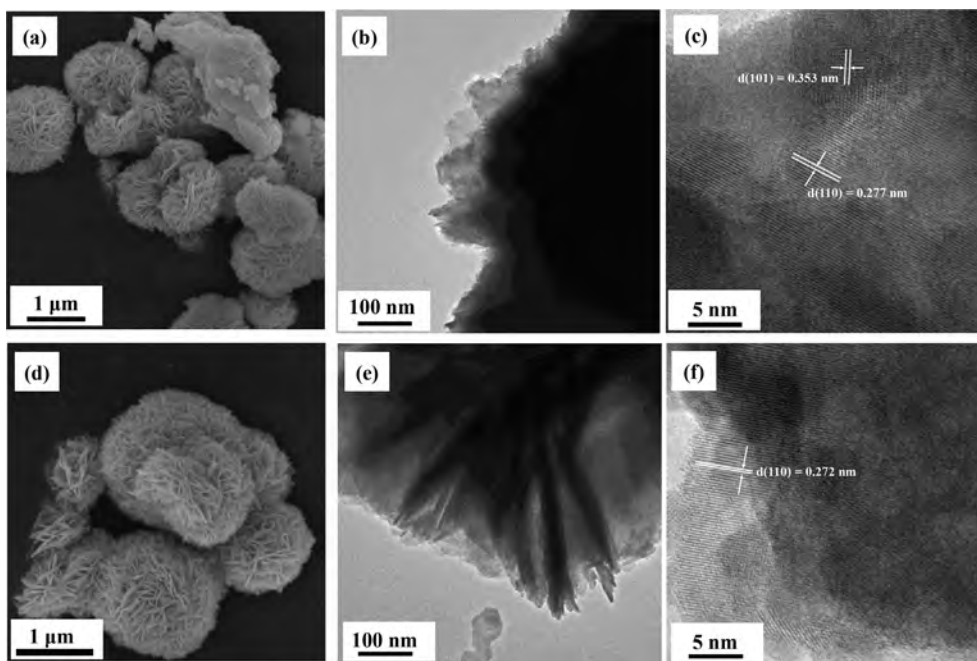
Fig. 1. (a) SEM of BiOBr; (b, c) Low- and high-resolution TEM of BiOBr; (d) SEM of 3% Cu-BiOBr; (e, f) Low- and high-resolution TEM of 3% Cu-BiOBr. In the high-resolution TEM images in (c, f), the lattice spacings of different planes of BiOBr are visible.

solvothermal method [50]. The introduction of Cu resulted in a higher ratio of Bi to Br (1.54), corroborating the replacement of Br by Cu (Table S2). In addition, the Cu amount in the BiOBr (Cu:Bi is 0.9%) was also calculated based on the XRF resultss.

TEM observations provide additional information regarding the interior structure of these materials. The low-resolution TEM (Fig. 1b and e) shows the similar edge of sample for BiOBr and 3% Cu-BiOBr. As shown in the high-resolution TEM in Fig. 1(c and f), the lattice fringes were typical of a highly crystalline species. As a result of Cu doping, there was slight decrease of the BiOBr (1 1 0) lattice spacing from 2.77 to 2.72 Å, as measured by TEM. To further explore the detailed structure of the photocatalysts, N_2 adsorption–desorption isotherms and the corresponding BJH pore size distributions were measured (Figs. S7 and S8). The curves of BiOBr and Cu-BiOBr (i.e., irrespective of the concentration of Cu) can be classified as type IV isotherms with H3 type hysteresis loops, indicating wide slit type mesopore. As shown in Fig. S8, the pore size of BiOBr and Cu-BiOBr were mainly distributed in 5.5 ~ 13.1 nm, suggesting the dominant presence of meso-pores (2 ~ 50 nm). Based on the unchanged surface area and pore type (see Table S3), the doping of Cu into BiOBr would not affect the surface characteristics considerably.

As shown in Fig. 2, the XRD patterns of the BiOBr samples with different levels of Cu doping exhibited the characteristic Bragg diffractions of tetragonal BiOBr (JCPDS 09–0393), indicating that the unique layered structure was retained after Cu doping. No diffraction peaks of any other phases or Cu-containing compounds were observed, suggesting that the doped Cu was highly dispersed within the BiOBr crystals. In contrast to pristine BiOBr, broadening of the major peaks (1 0 2) and (1 1 0) was observed in Cu-doped BiOBr, which indicated a decrease in crystallite size. The average crystallite size of pristine BiOBr as deduced from the Scherrer equation was approximately 45.7 nm, while the Cu-doped BiOBr samples had crystallite sizes of 35.5, 35.4, 34.8, 35.3 and 35.2 nm for 1%, 2%, 3%, 4% and 5% Cu dopant concentrations, respectively. Thus, the introduction of Cu^{2+} resulted in a lattice distortion which attenuated crystallite growth. Similar results have been reported for Al^{3+}- and Ti^{4+}-doped BiOBr [26,51].

The UV–vis diffuse reflectance absorption spectra of different samples are presented in Fig. 3a. As-obtained BiOBr possessed a sharp
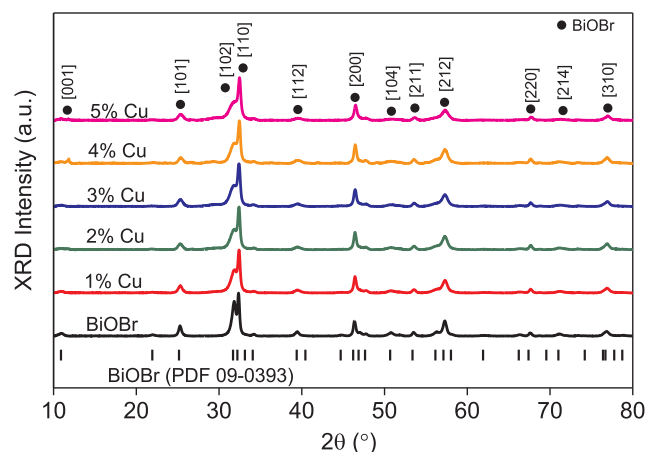

Fig. 2. XRD spectra of the undoped BiOBr and Cu-doped BiOBr with different doping levels between 10° and 80°. Also shown are the reference BiOBr diffraction peaks.

absorption edge at approximately 420 nm, and a broad absorbance beyond the edge which extended to about 600 nm, and which represented weakly defined low-energy sub-bandgap states commonly associated with oxygen vacancies and other extrinsic defects (Fig. 3b) [52]. The existence of oxygen vacancies in BiOBr has been reported to improve photocatalytic activity [53]. The Cu-doped BiOBr samples exhibited strong absorption bands at approximately 350 nm compared to the BiOBr matrix and a large absorption band between 550 nm and 800 nm, especially as dopant concentration increased (Fig. 3b). Additional charge transfer bands were attributed to the d–d transition of Cu^{2+} ($2E_g \rightarrow 2T_{2g}$) [54].

As shown in Fig. S9, the bandgap of pristine BiOBr was determined to be 2.92 eV, which was in agreement with the generally accepted bandgap of 2.70–2.95 eV. Further analysis of the XPS valence band spectra (Fig. S10) confirmed that the BiOBr had a valence band edge of 2.82 eV and a conduction band edge of −0.1 eV. With increasing concentrations of the Cu^{2+} dopant, the bandgap energy decreased and
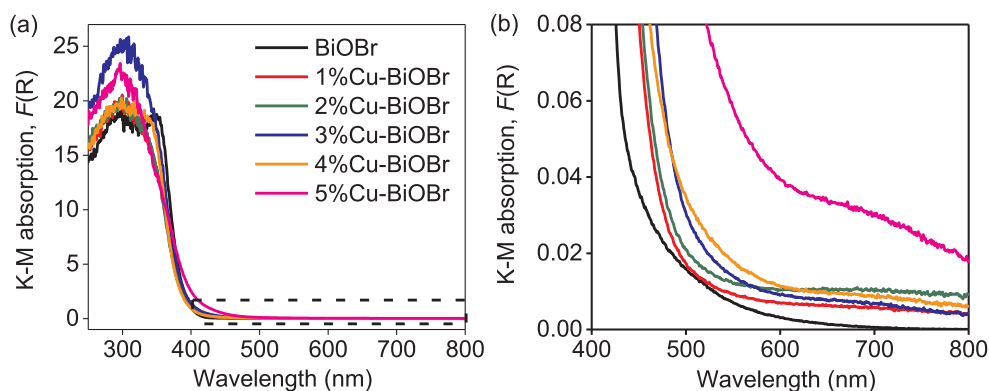
Fig. 3. (a) Kubelka-Munk absorbance and (b) the enlarged view from 400 to 800 nm.

was estimated to be 2.74 eV at the highest dopant concentration of 5 mol% (Fig. S9), implying that the presence of Cu^{2+} introduces mid-bandgap states in BiOBr, thus enabling the extrinsic photoexcitation. *Note*: The representative 3% Cu^{2+}-doped BiOBr was an optimised sample based on the photocatalytic assessment, as will be discussed later.

To further understand the Cu electronic levels in BiOBr, first-principles calculations were performed for the bulk BiOBr before and after Cu doping modification. Projected densities of states (PDOS) for BiOBr and Cu-doped BiOBr are shown in Fig. S11 and demonstrate that the intrinsic positions of the VB and CB remained almost unchanged after Cu-doping. An additional energy level appeared as the mid-gap state in the band gap of Cu-BiOBr, which was mainly contributed by Cu 4s orbitals, Bi 6s orbitals, Bi 6p orbitals and O 2p orbitals. Given that the VB maximum and CB minimum is 2.82 and −0.1 eV, respectively, the position of the Cu doping energy level was calculated to be 1.91 eV.

Photoluminescence (PL) spectroscopy was used to study the luminescence properties and the charge recombination phenomena of the semiconductor materials, which can yield information about the sub-bandgap defect states of BiOBr and Cu-doped BiOBr. Fig. 4 shows the fluorescence emission spectra of BiOBr and different Cu^{2+} doped BiOBr, obtained with 320 nm wavelength ultraviolet light as the excitation source. In the undoped BiOBr sample, one emission peak was observed at 418 nm and was assigned to the intrinsic band-edge emission (corresponding to a bandgap of approximately 2.97 eV). The other emission peaks (at 452, 469, 483 and 494 nm) were attributed to the different luminescent centres, such as defect energy levels attributable to bismuth interstitials and oxygen vacancies, as well as bonds dangling into nanocrystals [55].
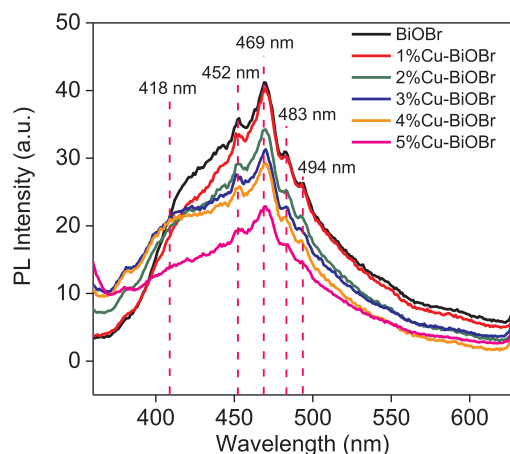

Fig. 4. Photoluminescence spectra of undoped and Cu-doped BiOBr at different doping levels.

PL intensity is known to generally be proportional to the recombination rate of photo-induced electron-hole pairs (semiconductor radiative recombination) [56]. In Fig. 4 it can be seen that the PL intensity steadily decreased as the of Cu^{2+} concentration in BiOBr increased, which suggested that the reduced recombination of electron/hole pairs resulted from the presence of various structural defects functioning as trap sites. The introduction of Cu^{2+} may thus increase the number of non-radiative transition centres and intrinsic defects, which decreases the PL intensity [57].

XPS measurements were used to obtain information regarding the elemental connectivity of the Cu-doped and undoped BiOBr samples. Peaks of Bi, O, Br and C could be clearly identified in the full scan spectra of the 3% Cu-BiOBr and BiOBr (Fig. S12), and all XPS spectra were corrected for specimen charging by referencing the C 1s peak to 284.60 eV. The peaks at binding energies around 159.2 eV and 165.3 eV corresponded to Bi $4f_{7/2}$ and Bi $4f_{5/2}$ [58], respectively, confirming the presence of Bi^{3+} in both samples (see Fig. 5a). The corresponding O 1s spectra for undoped and Cu-doped BiOBr (Fig. 5b) showed predominant contributions of lattice oxygen (O^{2-}) at 530.6 eV, the native defects of O^{2-} vacancies (OV) at 532.5 eV, and adsorbed H_2O at 533.8 eV [53]. The XPS spectra of Br 3d in the samples are shown in Fig. 5c. The peak can be deconvoluted into two peaks that correspond to Br $3d_{5/2}$ (68.3 eV) and Br $3d_{3/2}$ (69.5 eV), which are characteristic peaks of Br in BiOBr [59]. Both O 1s and Br 3d are shifted to a slightly lower binding energies with the doping of Cu into BiOBr, owing to the electronegativity of Cu (1.90) being lower than that of Br (2.96), meaning that substitution of Br with Cu generates higher electron density around O and Br.

Analysis of the Cu 2p of the Cu-doped BiOBr revealed the binding energy peak centred at 932.9 eV (Cu $2p_{3/2}$) and 952.5 eV (Cu $2p_{1/2}$), indicating the presence of a Cu^{2+} species (Fig. 5d) [60]. Given the relatively small amount of Cu in Cu-doped BiOBr, the peak at 941.4 eV was attributed to Bi 4s, although it was possible that this peak may have overlapped with Cu 2p satellite emissions [61]. In fact, the actual Cu loading in 3% Cu-doped BiOBr (Cu:Bi) is 0.9%, as determined by XRF techniques (Table S2). However, the Cu mol% values used in this study refer to the mol% of Cu in the prepared solutions.

3.2. Photocatalytic degradation of NOR

The effects of catalyst loading on photocatalytic degradation of NOR were investigated using concentrations of 3% Cu-doped BiOBr varying from 0.67 to 2 mg mL^{-1} (see Fig. 6). As expected, more NOR was adsorbed as the photocatalyst concentration increased, as shown in Fig. 6a. The kinetics of the photocatalytic degradation rate of NOR are determined using the Langmuir-Hinshelwood kinetics model, as given in the following (Eq. (1)):
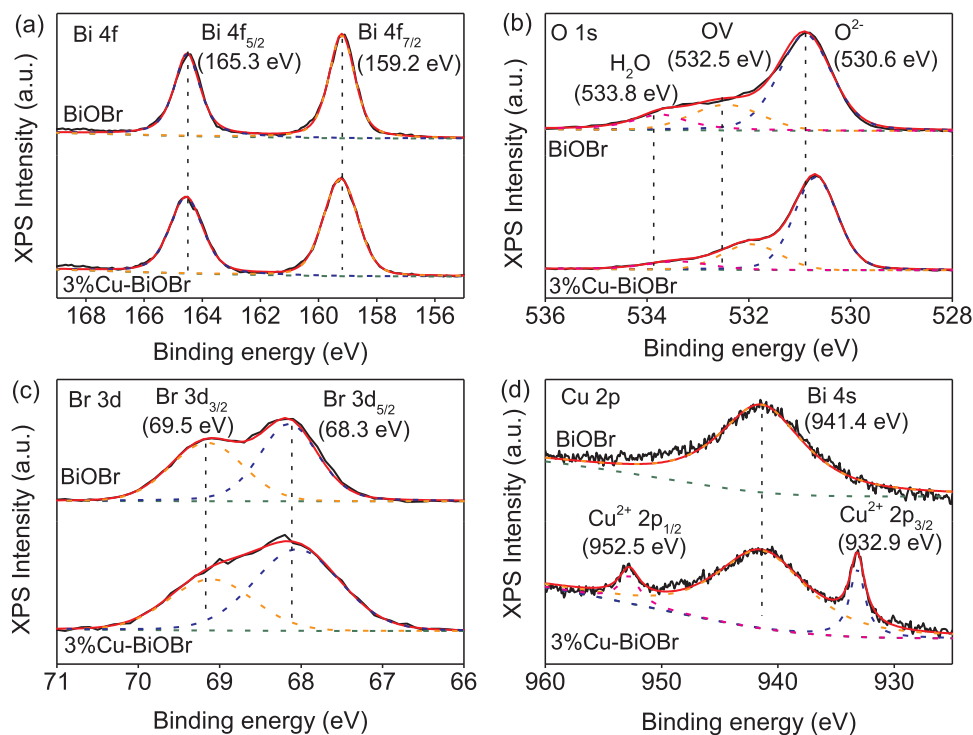
Fig. 5. XPS spectra for (a) Bi 4f, (b) O 1s, (c) Br 3d and (d) Cu 2p. Solid black lines show the measured data, while the solid red lines show the net sum of the deconvoluted peaks of various components (dashed lines). (For interpretation of the references to colour in this figure legend, the reader is referred to the web version of this article.)

$$-ln\frac{C}{C_i} = k_{app}t \tag{1}$$

where C is the concentration of NOR at different times and C_i is the concentration of NOR after dark adsorption. The pseudo-first-order rate constant, k_{app} (min^{-1}), was calculated from the slope of $-ln(C/C_i)$ versus irradiation time t. As shown in Fig. 6b and c, the initial rate of photocatalytic degradation increased when the concentration of 3% Cu-doped BiOBr was increased from 0.67 to 1.0 mg mL^{-1}, and then approached its maxima. It is well known that the rate of photoreaction initially increases with catalyst concentration, which is due to the larger absorbed photon flux by increasing photocatalyst concentrations. When the maximum rate constant becomes constant, it means that optimal light absorption has been reached. Normally, the photoreaction should be performed under this optimal light absorption condition because it significantly simplifies the interpretation of the photocatalytic mechanism to allow comparison of all the powders. Therefore, we choose 1 mg/mL as photocatalyst concentration for all the photocatalytic experiments to ensure a meaningful comparison. The effects of pH on photodegradation NOR was also investigated in Fig. S13, where weak acidic and neutral pH (5 ~ 7) is better than other conditions.

The adsorption of antibiotics on photocatalysts is another critical factor affecting the photocatalytic degradation rate, due to the low diffusion of the charge carriers into the solution [41,42]. Fig. 7 shows the adsorption profiles of NOR on BiOBr and different Cu-doped BiOBr samples. The same change was observed by FTIR before and after NOR adsorption on both BiOBr and Cu-doped BiOBr, as shown in Fig. S14, which indicated that the configuration of NOR on both sample surfaces was identical. To better understand the effect of different Cu doping in BiOBr on its adsorption performance for NOR, the Langmuir and Freundlich equation were used to fit the isotherms. The Langmuir and Freundlich models can be expressed respectively as follows:

$$q_e = \frac{q_m \alpha C_e}{1 + \alpha C_e} \tag{2}$$

$$q_e = K C_e^{1/n} \tag{3}$$

where q_e is the amount adsorbed in equilibrium with the concentration of adsorbate (mg/g), q_m is the maximum adsorption amount (mg/g), α is the Langmuir coefficient, C_e is equilibrium concentration of the NOR in the solution, K is the Freundlich adsorption constant and $1/n$ is the
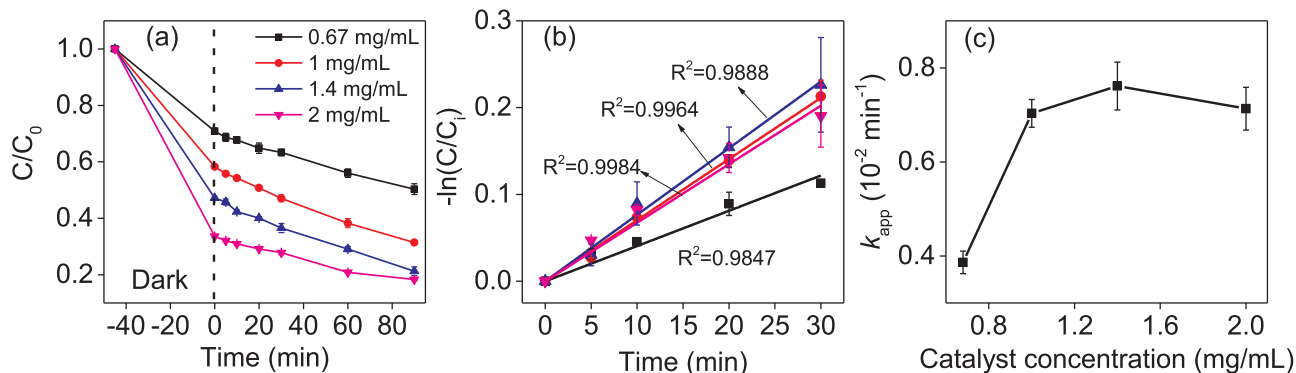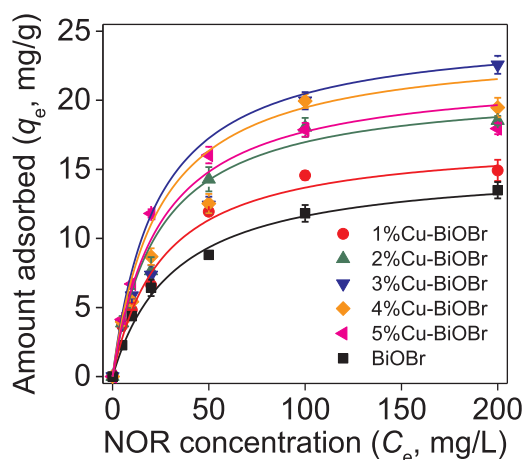

Fig. 6. (a) Photocatalytic degradation kinetics and (b) the corresponding Langmuir-Hinshelwood kinetics plot with different amounts of photocatalysts; and (c) the pseudo-first order constant (k_{app}) rate constant as a function of the catalyst amount.

T:\scanning\Elsevier\Journal\CEJ\126012\

Fig. 7. The adsorption isotherms of the BiOBr and Cu-doped BiOBr with different dopant concentrations.

coefficient (or degree) of linearity. The fitting of the curves can be found in Figs. S15 and S16 in supporting information and the parameters of the Langmuir and Freundlich isotherm equations is listed in Table 1. The experimental data obtained were correlated very well to the Langmuir model based on the high determination coefficients (R^2), indicating homogeneous distribution of adsorptive sites and monolayer adsorption. The results may arise from the limitation of the Freundlich isotherm, which can only accurately model the low concentration sub-saturation portion of the binding isotherm.

The NOR adsorption obtained from the Langmuir model indicated that the introduction of Cu^{2+} ions into BiOBr enhanced the adsorption capacity. The highest saturated adsorption (q_e) of NOR was obtained by 3% Cu-doped BiOBr and it would remain unchanged when the doping amount increases as shown in Table 1. The Langmuir coefficient, α, reflects the adsorbate-adsorbent interactions and is graphically reflected by the steepness of the linear rising region at low concentration. All the Cu-doped BiOBr samples show a higher α than the undoped one, indicating Cu doping may improve the adsorption kinetics.

Freundlich's n parameter relates to the mean energy of adsorption [62]. A strong adsorbent/adsorbate interaction occurs at values of n higher than 1, while values lower than 1 suggest a weak adsorbent/adsorbate interaction. Here, the n values for all Cu-doped BiOBr are higher than undoped one and 3% Cu-doped BiOBr has the highest n (2.24), which shows the same trend as the obtained from Langmuir coefficient. The enhanced adsorption capacity was again confirmed by the values of Freundlich's constant, K, as shown in Table 1. Based on the above results, the doping of Cu into BiOBr enhance the adsorption energy, which may further improve the photocatalytic activity.

We compared the photocatalytic degradation efficiency of NOR with the corresponding kinetic plots as a function of Cu^{2+} dopant

concentration (Fig. 8). The undoped BiOBr exhibited a relatively slower rate of degradation, especially under visible-light irradiation; this was a result of its large energy gap and limited visible-light absorption (Fig. 3). In contrast, a significant enhancement in the photocatalytic degradation rate of NOR was achieved over Cu^{2+}-doped samples. The maximal degradation rate was achieved in 3% Cu-doped BiOBr, which degraded NOR 1.22- and 2.28-fold faster than undoped BiOBr under full arc and visible light irradiation, respectively (Fig. 8b, d and Table 1). Further increasing the amount of Cu to 4%, the photodegradation decreased whether it was under visible light or full arc irradiation, which may be attributed to the dopant-induced defects which dominate and promote a faster charge recombination (form a recombination centre). It should be noted that the extent of the rate decrease under visible light is larger than that under full arc (Fig. 8b and d). Under full arc, the electrons will be excited from both the VB and Cu doping energy level to the CB of BiOBr as shown in Scheme 1b. However, the predominant photoelectrons come from the excitation of the Cu doping level under visible light irradiation (Scheme d). Therefore, when the dopants form the shallow level recombination centres (i.e. 4%Cu-BiOBr), the photo-excitation from the dopants level tend to be difficult, which results in a larger rate decrease under visible light irradiation. However, if the Cu amount further increases to 5%, deep level recombination centres form, which even trap the electrons from the intrinsic photoexcitation and thus result in a lower degradation rate than with the undoped BiOBr.

In addition, one should note that the photocatalytic degradation trend followed adsorption capacity, which was consistent with our expectation that adsorption was the limiting factor in the photocatalytic degradation of NOR. As shown in Table 1 and Fig. 8, with increasing Cu amounts, from 0 to 3%, NOR photodegradation rates increased from 0.28 to 0.64 min^{-1} and 10.37 to 12.63 min^{-1} for visible and full arc irradiation, respectively. These trends are in agreement with the Langmuir adsorption capacity (Fig. 7 and Table 1), justifying the requirement of adsorption for the direct hole transfer [63,64]. Further increases of the Cu amount to 5% will lead to a significant decrease in the degradation rate to 0.27 and 8.45 min^{-1} under visible and full arc irradiation, respectively. However, the adsorption capacity decreases only slightly from 23.81 to 22.94 mg/g as shown in Table 1. This again indicates that the formation of recombination centres at high Cu amounts. Because saturation of NOR on the BiOBr and Cu-doped BiOBr was achieved, their degradation rate constants are directly related to the turnover frequencies (TOFs, Table 1), which in this case, reflect the susceptibility of the NOR to being oxidized. The 3%Cu-BiOBr yields the highest TOFs, indicating the existence of Cu^{2+} does not only improve the adsorption capacity but also enhances the photocatalytic activity of each reaction sites due to the better separation efficiency of photo-charges.

Further photoelectrochemical experiments were done to investigate the effect of Cu^{2+} doping on BiOBr charge transfer characteristics [65]. Measurement of photocurrent was performed with BiOBr and a 3% Cu-doped BiOBr photoanode to more accurately determine the charge separation efficiency (Fig. S17a,b) [66]. The latter had a higher photocurrent under both visible light and full arc irradiation, which indicated that more holes were available for the degradation of NOR via a direct

Table 1
Parameters obtained by fitting of Langmuir and Freundlich equation; and photocatalytic degradation rate constants under full arc and visible light irradiation.

| Photocatalyst	Langmuir adsorption			Freundlich adsorption		k_{app} (10^{-2} min^{-1})		TOFs (10^{-6} s^{-1})	
	α	q_e (mg/g)	N (10^{19} g^{-1})	K (mg/g)	n	Visible	Full arc	Visible	Full arc
BiOBr	0.035	15.87	2.99	1.06	1.95	0.28	10.37	4.81	76.4
1%Cu-BiOBr	0.038	18.14	3.42	1.78	2.08	0.39	10.38	6.29	80.1
2%Cu-BiOBr	0.041	21.05	3.97	1.97	2.22	0.61	11.78	6.45	81.4
3% Cu-BiOBr	0.043	23.81	4.49	2.24	2.24	0.64	12.63	6.61	82.6
4%Cu-BiOBr	0.042	23.14	4.37	2.14	2.19	0.58	12.50	4.45	79.2
5%Cu-BiOBr	0.041	22.94	4.14	2.13	2.18	0.27	8.45	3.11	46.5
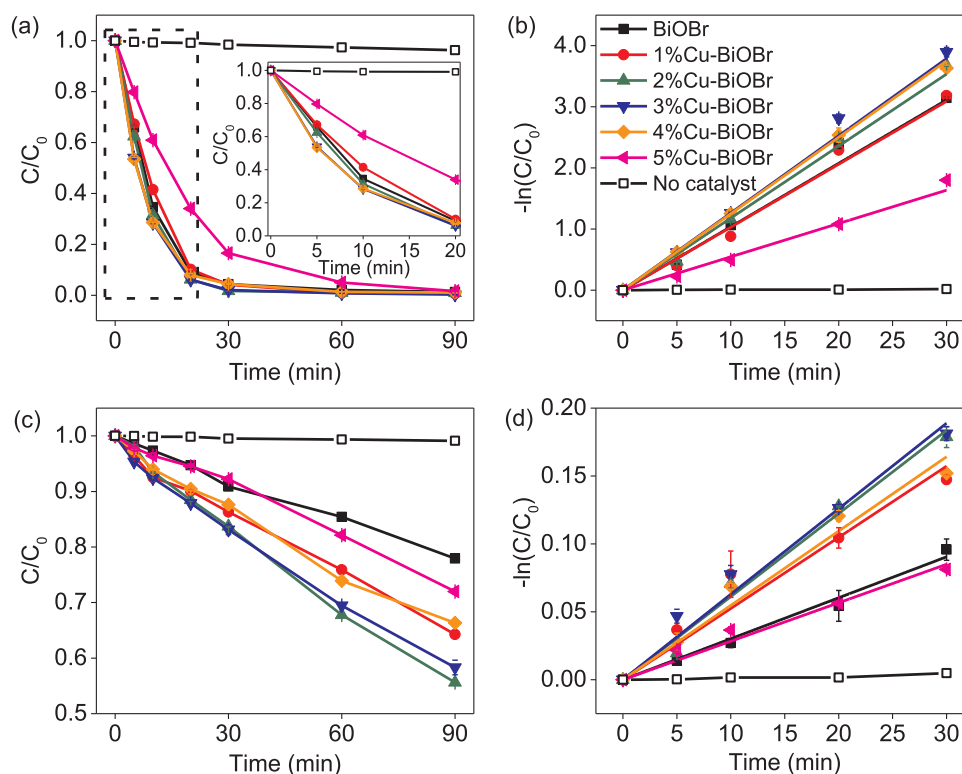
Fig. 8. Degradation kinetics of NOR over pristine BiOBr and Cu-doped BiOBr at different doping amounts under (a) full arc and (c) visible light ($\lambda \geq 420$ nm). (b, d) The corresponding Langmuir-Hinshelwood kinetics plot derived from (a) and (c), respectively. Photocatalyst loading: 1 mg mL^{-1}.

NOR = Norfloxacin
NOR$^+$ = Oxidised products of norfloxacin
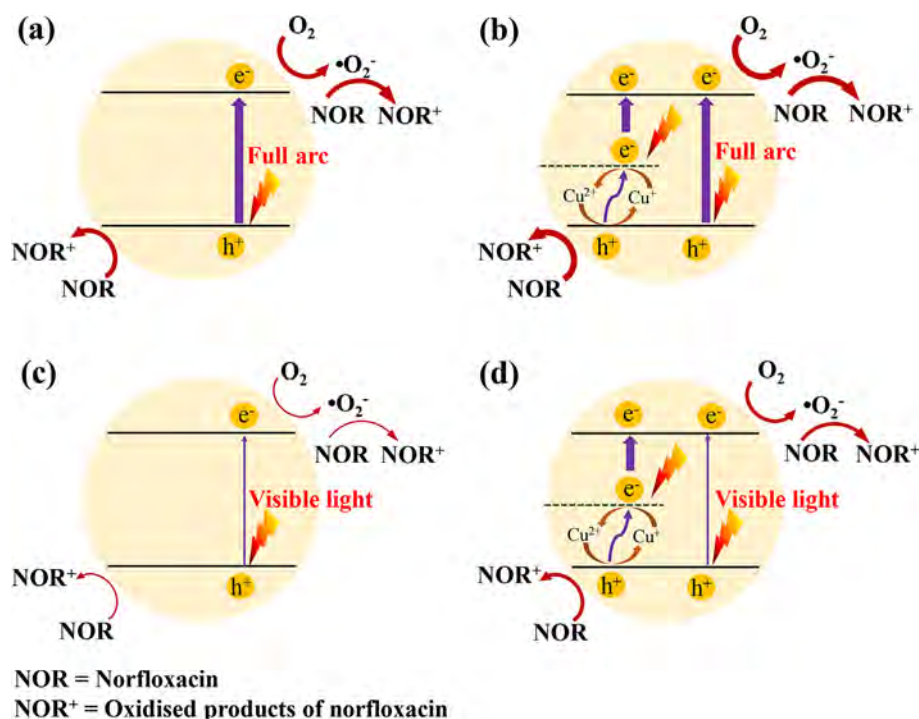
Scheme 1. Mechanistics of photocharge transport and surface transfer on (a, c) BiOBr and (b, d) Cu-BiOBr in presence of NOR and dissolved oxygen under (a, b) full arc and (c, d) visible light irradiation. The thickness of arrows represents the densities of photocharge transport in each step.

hole-oxidation pathway (which will be discussed later). The electrochemical impedance (EIS) of two photocatalysts were also compared to study the surface charge-transfer process (Fig. S18a,b). The EIS spectrum of 3% Cu-doped BiOBr exhibited a smaller interfacial charge-transfer resistance, indicating that charge-transfer was faster from the photocatalyst surface to the reductant in the electrolyte, which was in agreement with our photocatalytic results. Additionally, it is generally accepted that the characteristic frequency peak in Bode phase plots tends to be relevant to the inverse of the electron lifetime [67]. Correspondingly, from the Bode phase plots in Fig. S18c and d, we can see

that 3% Cu-BiOBr has a characteristic frequency peak at 1.135 Hz, which is lower than undoped BiOBr at 1.163 Hz. The same trends can be observed under full arc irradiation. This implies that the doping of Cu can inhibit the recombination of electron-hole pairs.

The degradation of NOR mainly involved piperazine ring transformation, defluorination and decarboxylation [68]. In our study, the transformation of the piperazine ring played the major role in the photocatalytic degradation process and four intermediates were identified as shown in Table S4 and Fig. S19. The existence of intermediates further resulted in an unchanged TOC as shown in Fig. S20. Based on the previous reports, the transformation and oxidation of the piperazine ring resulted in a lower steric resistance and easier penetration into the cells of luminescent bacteria, leading to the increase of toxicity [69,70]. However, the intermediates exerted lower toxicity on the bacteria after a long photodegradation time [71]. Despite this, one should take care to evaluate the intermediates/products after long irradiation times because it may cause other oxygenated organic compounds to form [72]. After the photodegradation, metal leaching from the catalyst was measured to be 197 ppb and 93 ppb for Cu^{2+} and Bi^{3+}, respectively, which is well below the threshold permitted value for Cu (1 ppm) and Bi (15 ppm) according to the Environmental Protection Agency.

3.3. Reactive species and possible mechanism

The effects of various radical scavengers on the degradation of NOR were investigated to examine the underlying photodegradation mechanism. Potassium iodide (KI) [73], isopropanol (IPA) [74] and benzoquinone (BQ) [75] were added to the reaction system as holes (h^+), hydroxide radicals ($\cdot OH^-$) and superoxide radicals ($\cdot O_2^-$) scavenger, respectively. Fig. 9 compares the variation of degradation kinetics and pseudo-first-order rate constants in the presence of these scavengers. NOR was completely degraded in the absence of scavengers within 30 min under full arc irradiation with a rate constant of 0.131 min^{-1}. When KI was added to the NOR solution to give a concentration of 0.31 mM KI (10 times larger than the concentration of NOR), there was complete inhibition of NOR degradation until after 30 min of

irradiation had been conducted (Fig. 9a, d). When the KI concentration was decreased to 0.15 and 0.062 mM, the inhibition was assessed to be 93.9% (0.008 min^{-1}) and 77.3% (0.0298 min^{-1}), respectively.

With the addition of an $\cdot O_2^-$ scavenger, i.e., BQ, the same effect was observed but to a lesser extent, with 93.2% (0.008 min^{-1}), 71.7% (0.037 min^{-1}) and 41.2% (0.077 min^{-1}) inhibition achieved for 0.31, 0.15 and 0.062 mM BQ, respectively. This suggested that the photodegradation of NOR by superoxide radicals was not the only mechanism at play. In contrast, the addition of 31 mM IPA (1000 times larger than the concentration of NOR) as an $\cdot OH^-$ scavenger had a negligible effect on the k_{app} of NOR degradation compared with no scavenger, indicating that $\cdot OH^-$ was not the main reactive species. Based on these results, it was concluded that the degradation of NOR was mainly mediated by direct hole oxidation. At this juncture, we could not exclude that the oxidation of NOR as a possible rate-determining pathway, performed by superoxide radicals that formed from a one-electron reduction reaction ($E°(O_2/\cdot O_2^-) = +0.133$ V vs RHE, pH 0). Under visible light irradiation, the main species were found still to be photoholes (Fig. S21), indicating the same NOR degradation mechanism.

On the basis of the aforementioned results, the photocatalytic NOR degradation process with the BiOBr and Cu-BiOBr has been elucidated and illustrated in Scheme 1. Because of the formation of the doping level in the band gap of Cu-BiOBr, the electrons in VB were transited into the Cu doping energy level by the interconversion between Cu^+ and Cu^{2+}. Under full arc irradiation (Scheme 1b), the electrons (in VB of Cu-BiOBr and Cu doping energy level) were excited to CB and react with dissolved oxygen, which in turn means more photoholes would be used to degrade NOR than with undoped BiOBr. Under visible light irradiation (Scheme 1d), the predominant contribution for degradation of NOR with Cu-BiOBr came from the excitation of Cu doping energy level since the large band gap of BiOBr. Therefore, the introduction of Cu into BiOBr shows higher NOR degradation enhancement under visible light (2.28 times higher than undoped BiOBr) than that of full arc irradiation (1.22 times higher than undoped BiOBr).
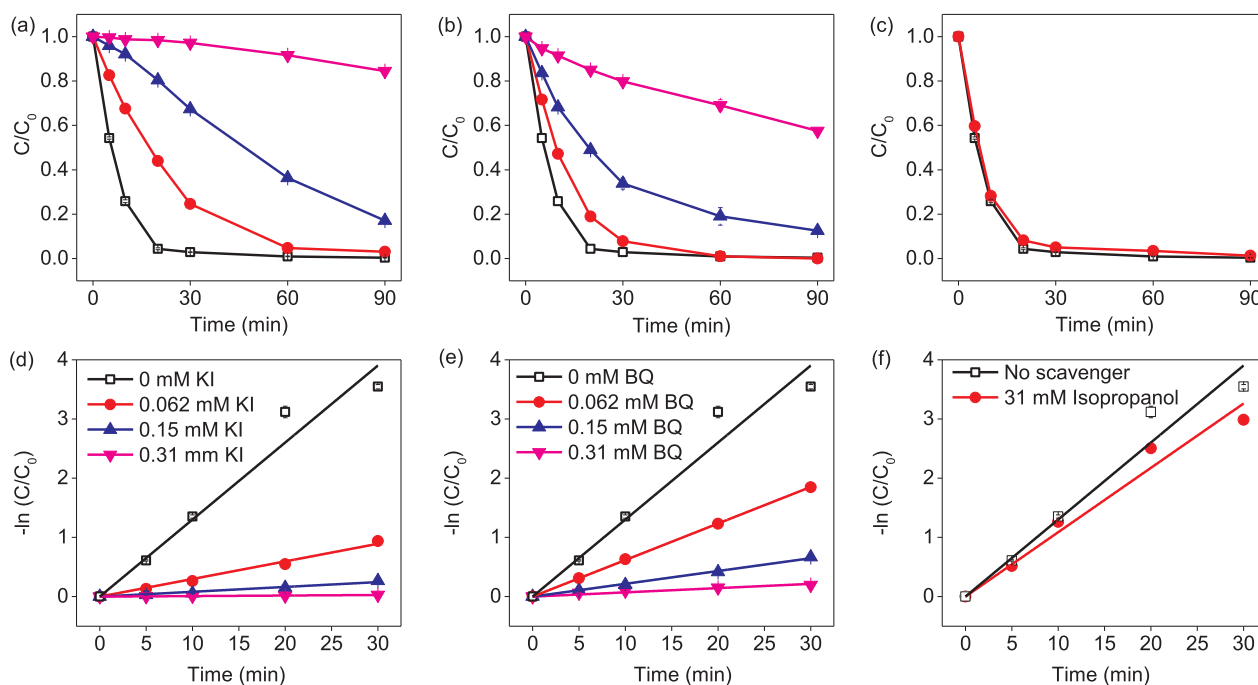

Fig. 9. Photocatalytic degradation kinetics of NOR in the presence of various scavengers: (a) various concentrations of KI, (b) various concentrations of BQ and (c) isopropanol. (d–f) the corresponding Langmuir-Hinshelwood kinetics plot. Photocatalyst loading: 1 mg mL^{-1} 3% Cu-doped BiOBr; initial concentration of NOR: 10 ppm; light source: full arc. All experiments were performed in the presence of dissolved oxygen.
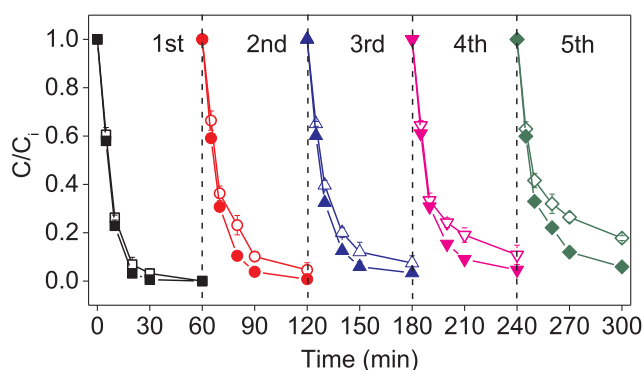
Fig. 10. The repeated photocatalytic degradation of norfloxacin (NOR) over 3% Cu-doped BiOBr (open symbol) and regenerated 3% Cu-doped BiOBr (solid symbol). Photocatalyst loading: 1 mg mL^{-1}, light source: full arc light.

3.4. The reusability of photocatalyst

In addition to its photocatalytic efficiency, the reusability of a photocatalyst is also very important for practical applications. To evaluate the reusability of 3% Cu-doped BiOBr, five successive photocatalytic experimental runs were conducted by adding the same overall concentrations of recycled 3% Cu-doped BiOBr photocatalyst (Fig. 10 open symbol) or regenerated photocatalyst (Fig. 10 solid symbol) after each reaction cycle to fresh NOR solutions under full arc irradiation.

As shown in Fig. 10, it was found that the photocatalytic activity of 3% Cu-BiOBr (open symbol) retained 80% of its initial activity after five photodegradation cycles. The loss of photocatalytic activity may be attributed to the adsorption of the remaining NOR and intermediates on the photocatalyst surface during the repeated experiments, which was estimated by FTIR (Fig. S22) and TG analysis (Fig. S23). The weight of the pure Cu-doped BiOBr decreased markedly from 600 °C to 700 °C, owing to the degradation and formation of Bi_2O_3, while the TG analysis curve for Cu-doped BiOBr after photodegradation showed a progressive weight loss at 220 °C with a clear shoulder at 100 °C, which indicated the removal of physisorbed water, while the weight loss from 200 to 250 °C represented the complete decomposition of intermediate structure, resulting in the formation of CO_2. To rule out the effect of adsorbed intermediates, the regenerated 3%Cu-BiOBr was prepared by sintering it at 250 °C for 1 h after each photodegradation cycle. As shown in Fig. 10 (solid symbol), the photocatalytic activity of the fifth cycle was an impressive 95% of the first cycle. The XRD pattern (Fig. S24) of the regenerated sample before and after photodegradation illustrated that the crystal structure of 3% Cu-doped BiOBr remained unchanged, which indicated that the 3% Cu-doped BiOBr may be a durable and practical photocatalyst for the remediation of NOR-containing water samples.

4. Conclusions

This study demonstrated the advantage of Cu-doping BiOBr to impart materials with enhanced photocatalytic activities in visible light and improved adsorption capacity towards NOR. Optimisation of the doping amount revealed that 3% Cu-doped BiOBr enhanced the photocatalytic activity of BiOBr in degradation of NOR by more than two-fold. Cu-dopant helped increase the net charge-separation and surface charge transfer. The improved NOR adsorption on this photocatalyst is key factor that contributed to the improved photocatalytic activity. Photogenerated h$^+$ were shown to be the major reactive species responsible for the degradation of NOR in the Cu-doped BiOBr photocatalytic system. Cu-doped BiOBr demonstrated high reusability throughout five successive catalytic cycles. This research will be invaluable for the practical application of BiOBr in the field of photocatalysis and has also enhanced the understanding of the associated

photophysical and photochemical processes underlying this phenomenon.

Declaration of Competing Interest

The authors declare that they have no known competing financial interests or personal relationships that could have appeared to influence the work reported in this paper.

Acknowledgements

Appendix A. Supplementary data

Supplementary data to this article can be found online at https://doi.org/10.1016/j.cej.2020.126012.

References

[1] C. Liu, V. Nanaboina, G.V. Korshin, W. Jiang, Spectroscopic study of degradation products of ciprofloxacin, norfloxacin and lomefloxacin formed in ozonated wastewater, Water Res. 46 (2012) 5235–5246, https://doi.org/10.1016/j.watres.2012.07.005.

[2] R.A. Brain, D.J. Johnson, S.M. Richards, H. Sanderson, P.K. Sibley, K.R. Solomon, Effects of 25 pharmaceutical compounds to Lemna gibba using a seven-day static-renewal test, Environ. Toxicol. Chem. 23 (2004) 371–382, https://doi.org/10.1897/02-576.

[3] A.A. Robinson, J.B. Belden, M.J. Lydy, Toxicity of fluoroquinolone antibiotics to aquatic organisms, Environ. Toxicol. Chem. 24 (2005) 423–430, https://doi.org/10.1897/04-210R.1.

[4] H. Peng, S. Feng, X. Zhang, Y. Li, X. Zhang, Adsorption of norfloxacin onto titanium oxide: effect of drug carrier and dissolved humic acid, Sci. Total Environ. 438 (2012) 66–71, https://doi.org/10.1016/j.scitotenv.2012.08.045.

[5] S.D. Jojoa-Sierra, J. Silva-Agredo, E. Herrera-Calderon, R.A. Torres-Palma, Elimination of the antibiotic norfloxacin in municipal wastewater, urine and seawater by electrochemical oxidation on IrO$_2$ anodes, Sci. Total Environ. 575 (2017) 1228–1238, https://doi.org/10.1016/j.scitotenv.2016.09.201.

[6] J. Rivas, Á. Encinas, F. Beltrán, N. Graham, Application of advanced oxidation processes to doxycycline and norfloxacin removal from water, J. Environ. Sci. Health A 46 (2011) 944–951, https://doi.org/10.1080/10934529.2011.586249.

[7] V.R. Ferreira, C.L. Amorim, S.M. Cravo, M.E. Tiritan, P.M. Castro, C.M. Afonso, Fluoroquinolones biosorption onto microbial biomass: activated sludge and aerobic granular sludge, Int. Biodeterior. Biodegrad. 110 (2016) 53–60, https://doi.org/10.1016/j.ibiod.2016.02.014.

[8] B. Pan, B. Xing, Adsorption mechanisms of organic chemicals on carbon nanotubes, Environ. Sci. Technol. 42 (2008) 9005–9013, https://doi.org/10.1021/es801777n.

[9] X. Wu, M. Huang, T. Zhou, J. Mao, Recognizing removal of norfloxacin by novel magnetic molecular imprinted chitosan/γ-Fe$_2$O$_3$ composites: selective adsorption mechanisms, practical application and regeneration, Sep. Purif. Technol. 165 (2016) 92–100, https://doi.org/10.1016/j.seppur.2016.03.041.

[10] D.A. Coledam, J.M. Aquino, B.F. Silva, A.J. Silva, R.C. Rocha-Filho, Electrochemical mineralization of norfloxacin using distinct boron-doped diamond anodes in a filter-press reactor, with investigations of toxicity and oxidation by-products, Electrochim. Acta 213 (2016) 856–864, https://doi.org/10.1016/j.electacta.2016.08.003.

[11] G. Boczkaj, A. Fernandes, Wastewater treatment by means of advanced oxidation processes at basic pH conditions: a review, Chem. Eng. J. 320 (2017) 608–633, https://doi.org/10.1016/j.cej.2017.03.084.

[12] M. Gągol, A. Przyjazny, G. Boczkaj, Wastewater treatment by means of advanced oxidation processes based on cavitation–a review, Chem. Eng. J. 338 (2018) 599–627, https://doi.org/10.1016/j.cej.2018.01.049.

[13] R. Yuan, Z. Jiang, Z. Wang, S. Gao, Z. Liu, M. Li, G. Boczkaj, Hierarchical MnO$_2$ nanoflowers blooming on 3D nickel foam: a novel micro-macro catalyst for peroxymonosulfate activation, J. Colloid Interface Sci. (2020), https://doi.org/10.1016/j.jcis.2020.03.041.

[14] R. Yuan, M. Jiang, S. Gao, Z. Wang, H. Wang, G. Boczkaj, Z. Liu, J. Ma, Z. Li, 3D mesoporous α-Co(OH)$_2$ nanosheets electrodeposited on nickel foam: a new generation of macroscopic cobalt-based hybrid for peroxymonosulfate activation, Chem. Eng. J. 380 (2020) 122447, , https://doi.org/10.1016/j.cej.2019.122447.

[15] A. Fernandes, P. Makoś, G. Boczkaj, Treatment of bitumen post oxidative effluents by sulfate radicals based advanced oxidation processes (S-AOPs) under alkaline pH conditions, J. Clean. Prod. 195 (2018) 374–384, https://doi.org/10.1016/j.jclepro.2018.05.207.

[16] A. Fernandes, P. Makoś, Z. Wang, G. Boczkaj, Synergistic effect of TiO$_2$

photocatalytic advanced oxidation processes in the treatment of refinery effluents, Chem. Eng. J. 123488 (2019), https://doi.org/10.1016/j.cej.2019.123488.

[17] A. Fernandes, M. Gągol, P. Makoś, J.A. Khan, G. Boczkaj, Integrated photocatalytic advanced oxidation system (TiO$_2$/UV/O$_3$/H$_2$O$_2$) for degradation of volatile organic compounds, Sep. Purif. Technol. 224 (2019) 1–14, https://doi.org/10.1016/j.seppur.2019.05.012.

[18] M. Chen, W. Chu, Degradation of antibiotic norfloxacin in aqueous solution by visible-light-mediated C-TiO$_2$ photocatalysis, J. Hazard. Mater. 219 (2012) 183–189, https://doi.org/10.1016/j.jhazmat.2012.03.074.

[19] J. Gou, Q. Ma, X. Deng, Y. Cui, H. Zhang, X. Cheng, X. Li, M. Xie, Q. Cheng, Fabrication of Ag$_2$O/TiO$_2$-Zeolite composite and its enhanced solar light photocatalytic performance and mechanism for degradation of norfloxacin, Chem. Eng. J. 308 (2017) 818–826, https://doi.org/10.1016/j.cej.2016.09.089.

[20] N.S. Shah, J.A. Khan, M. Sayed, Z.U.H. Khan, A.D. Rizwan, N. Muhammad, G. Boczkaj, B. Murtaza, M. Imran, H.M. Khan, Solar light driven degradation of norfloxacin using as-synthesized Bi^{3+} and Fe^{2+} co-doped ZnO with the addition of HSO$_5^-$: toxicities and degradation pathways investigation, Chem. Eng. J. 351 (2018) 841–855, https://doi.org/10.1016/j.cej.2018.06.111.

[21] R.D.C. Soltani, M. Mashayekhi, M. Naderi, G. Boczkaj, S. Jorfi, M. Safari, Sonocatalytic degradation of tetracycline antibiotic using zinc oxide nanostructures loaded on nano-cellulose from waste straw as nanosonocatalyst, Ultrason. Sonochem. 55 (2019) 117–124, https://doi.org/10.1016/j.ultsonch.2019.03.009.

[22] R.D.C. Soltani, Z. Miraftabi, M. Mahmoudi, S. Jorfi, G. Boczkaj, A. Khataee, Stone cutting industry waste-supported zinc oxide nanostructures for ultrasonic assisted decomposition of an anti-inflammatory non-steroidal pharmaceutical compound, Ultrason. Sonochem. 58 (2019) 104669, , https://doi.org/10.1016/j.ultsonch.2019.104669.

[23] X. Chen, A. Selloni, Introduction: titanium dioxide (TiO$_2$) nanomaterials, Chem. Rev. 114 (2014) 9281–9282, https://doi.org/10.1021/cr500422r.

[24] H. Sun, S. Liu, S. Liu, S. Wang, A comparative study of reduced graphene oxide modified TiO$_2$, ZnO and Ta$_2$O$_5$ in visible light photocatalytic/photochemical oxidation of methylene blue, Appl. Catal. B: Environ 146 (2014) 162–168, https://doi.org/10.1016/j.apcatb.2013.03.027.

[25] M. Shang, W. Wang, L. Zhang, Preparation of BiOBr lamellar structure with high photocatalytic activity by CTAB as Br source and template, J. Hazard. Mater. 167 (2009) 803–809, https://doi.org/10.1016/j.jhazmat.2009.01.053.

[26] R. Wang, G. Jiang, X. Wang, R. Hu, X. Xi, S. Bao, Y. Zhou, T. Tong, S. Wang, T. Wang, Efficient visible-light-induced photocatalytic activity over the novel Ti-doped BiOBr microspheres, Powder Technol. 228 (2012) 258–263, https://doi.org/10.1016/j.powtec.2012.05.028.

[27] H. Cheng, B. Huang, P. Wang, Z. Wang, Z. Lou, J. Wang, X. Qin, X. Zhang, Y. Dai, In situ ion exchange synthesis of the novel Ag/AgBr/BiOBr hybrid with highly efficient decontamination of pollutants, Chem. Commun. 47 (2011) 7054–7056, https://doi.org/10.1039/C1CC11525A.

[28] J. Xu, W. Meng, Y. Zhang, L. Li, C. Guo, Photocatalytic degradation of tetra-bromobisphenol A by mesoporous BiOBr: efficacy, products and pathway, Appl. Catal. B: Environ 107 (2011) 355–362, https://doi.org/10.1016/j.apcatb.2011.07.036.

[29] X. Zhang, Z. Ai, F. Jia, L. Zhang, Generalized one-pot synthesis, characterization, and photocatalytic activity of hierarchical BiOX (X= Cl, Br, I) nanoplate microspheres, J. Phys. Chem. C 112 (2008) 747–753, https://doi.org/10.1021/jp077471t.

[30] K. Yu, S. Yang, H. He, C. Sun, C. Gu, Y. Ju, Visible light-driven photocatalytic degradation of rhodamine B over NaBiO$_3$: pathways and mechanism, J. Phys. Chem. A 113 (2009) 10024–10032, https://doi.org/10.1021/jp905173e.

[31] Z. Ai, J. Wang, L. Zhang, Substrate-dependent photoreactivities of BiOBr nanoplates prepared at different pH values, Chin. J. Catal. 36 (2015) 2145–2154, https://doi.org/10.1016/S1872-2067(15)60986-X.

[32] G. Jiang, X. Wang, Z. Wei, X. Li, X. Xi, R. Hu, B. Tang, R. Wang, S. Wang, T. Wang, Photocatalytic properties of hierarchical structures based on Fe-doped BiOBr hollow microspheres, J. Mater. Chem. A 1 (2013) 2406–2410, https://doi.org/10.1039/c2ta00942k.

[33] H. Lin, X. Li, J. Cao, S. Chen, Y. Chen, Novel I$^-$-doped BiOBr composites: modulated valence bands and largely enhanced visible light phtotocatalytic activities, Catal. Commun. 49 (2014) 87–91, https://doi.org/10.1016/j.catcom.2014.02.010.

[34] D. Wu, S. Yue, W. Wang, T. An, G. Li, H.Y. Yip, H. Zhao, P.K. Wong, Boron doped BiOBr nanosheets with enhanced photocatalytic inactivation of Escherichia coli, Appl. Catal. B: Environ. 192 (2016) 35–45, https://doi.org/10.1016/j.apcatb.2016.03.046.

[35] M. Guo, J. Du, First-principles study of electronic structures and optical properties of Cu, Ag, and Au-doped anatase TiO$_2$, Phys. B: Condensed Matter 407 (2012) 1003–1007, https://doi.org/10.1016/j.physb.2011.12.128.

[36] M. Ferhat, A. Zaoui, R. Ahuja, Magnetism and band gap narrowing in Cu-doped ZnO, Appl. Phys. Lett. 94 (2009) 142502, , https://doi.org/10.1063/1.3112603.

[37] B. Babu, A. Kadam, R. Ravikumar, C. Byon, Enhanced visible light photocatalytic activity of Cu-doped SnO$_2$ quantum dots by solution combustion synthesis, J. Alloys Compd. 703 (2017) 330–336, https://doi.org/10.1016/j.jallcom.2017.01.311.

[38] W. Qin, J. Qi, X. Wu, Photocatalytic property of Cu^{2+}-doped Bi$_2$O$_3$ films under visible light prepared by the sol–gel method, Vacuum 107 (2014) 204–207, https://doi.org/10.1016/j.vacuum.2014.02.003.

[39] Y. Liu, Q. Wu, One novel material with high visible-light activity: hexagonal Cu flakelets embedded in the petals of BiOBr flower-nanospheres, J. Nanopart. Res. 19 (2017) 516, https://doi.org/10.1007/s11051-016-3734-1).

[40] W. Li, Y. Zou, X. Geng, F. Xiao, G. An, D. Wang, Constructing highly catalytic oxidation over BiOBr-based hierarchical microspheres: importance of redox potential of doped cations, Mol. Catal. 438 (2017) 19–29, https://doi.org/10.1016/j.mcat.2017.05.017.

[41] J. Schwitzgebel, J.G. Ekerdt, H. Gerischer, A. Heller, Role of the oxygen molecule and of the photogenerated electron in TiO$_2$-photocatalyzed air oxidation reactions, J. Phys. Chem. 99 (1995) 5633–5638, https://doi.org/10.1021/j100015a055.

[42] K.-I. Ishibashi, A. Fujishima, T. Watanabe, K. Hashimoto, Generation and deactivation processes of superoxide formed on TiO$_2$ film illuminated by very weak UV light in air or water, J. Phys. Chem. B 104 (2000) 4934–4938, https://doi.org/10.1021/jp9942670.

[43] S.P. Patil, R.P. Patil, V.K. Mahajan, G. Sonawane, V. Shrivastava, S. Sonawane, Facile sonochemical synthesis of BiOBr-graphene oxide nanocomposite with enhanced photocatalytic activity for the degradation of direct green, Mater. Sci. Semicond. Process. 52 (2016) 55–61, https://doi.org/10.1016/j.mssp.2016.05.008.

[44] J. Zhang, F. Shi, J. Lin, D. Chen, J. Gao, Z. Huang, X. Ding, C. Tang, Self-assembled 3-D architectures of BiOBr as a visible light-driven photocatalyst, Chem. Mater. 20 (2008) 2937–2941, https://doi.org/10.1021/cm7031898.

[45] G. Kresse, J. Furthmüller, Efficient iterative schemes for ab initio total-energy calculations using a plane-wave basis set, Phys. Rev. B 54 (1996) 11169, https://doi.org/10.1103/PhysRevB.54.11169.

[46] P.E. Blöchl, Projector augmented-wave method, Phys. Rev. B 50 (1994) 17953, https://doi.org/10.1103/PhysRevB.50.17953.

[47] J.P. Perdew, K. Burke, M. Ernzerhof, Generalized gradient approximation made simple, Phys. Rev. Lett. 77 (1996) 3865, https://doi.org/10.1103/PhysRevLett.77.3865.

[48] Y. Wang, S. Lany, J. Ghanbaja, Y. Fagot-Revurat, Y. Chen, F. Soldera, D. Horwat, F. Mücklich, J. Pierson, Electronic structures of Cu$_2$O, Cu$_4$O$_3$, and CuO: a joint experimental and theoretical study, Phys. Rev. B 94 (2016) 245418, , https://doi.org/10.1103/PhysRevB.94.245418.

[49] M. Song, M. Du, Q. Liu, F. Xing, C. Huang, X. Qiu, Enhancement of photocatalytic activities in hierarchical BiOBr microflowers induced by oxygen vacancies, Catal. Today 335 (2019) 193–199, https://doi.org/10.1016/j.cattod.2018.11.006.

[50] C. Xue, J. Xia, T. Wang, S. Zhao, G. Yang, B. Yang, Y. Dai, G. Yang, A facile and efficient solvothermal fabrication of three-dimensionally hierarchical BiOBr microspheres with exceptional photocatalytic activity, Mater. Lett. 133 (2014) 274–277, https://doi.org/10.1016/j.matlet.2014.07.016.

[51] Z. Liu, B. Wu, Y. Zhao, J. Niu, Y. Zhu, Solvothermal synthesis and photocatalytic activity of Al-doped BiOBr microspheres, Ceram. Int. 40 (2014) 5597–5603, https://doi.org/10.1016/j.ceramint.2013.10.152.

[52] X. Wu, K. Zhang, G. Zhang, S. Yin, Facile preparation of BiOX (X= Cl, Br, I) nanoparticles and up-conversion phosphors/BiOBr composites for efficient degradation of NO gas: oxygen vacancy effect and near infrared light responsive mechanism, Chem. Eng. J. 325 (2017) 59–70, https://doi.org/10.1016/j.cej.2017.05.044.

[53] H. Wang, D. Yong, S. Chen, S. Jiang, X. Zhang, W. Shao, Q. Zhang, W. Yan, B. Pan, Y. Xie, Oxygen-vacancy-mediated exciton dissociation in BiOBr for boosting charge-carrier-involved molecular oxygen activation, J. Am. Chem. Soc. 140 (2018) 1760–1766, https://doi.org/10.1021/jacs.7b10997.

[54] H. Praliaud, S. Mikhailenko, Z. Chajar, M. Primet, Surface and bulk properties of Cu–ZSM-5 and Cu/Al$_2$O$_3$ solids during redox treatments. Correlation with the selective reduction of nitric oxide by hydrocarbons, Appl. Catal. B: Environ. 16 (1998) 359–374, https://doi.org/10.1016/S0926-3373(97)00093-3.

[55] M. Gao, D. Zhang, X. Pu, H. Li, D. Lv, B. Zhang, X. Shao, Facile hydrothermal synthesis of Bi/BiOBr composites with enhanced visible-light photocatalytic activities for the degradation of rhodamine B, Sep. Purif. Technol. 154 (2015) 211–216, https://doi.org/10.1016/j.seppur.2015.09.063.

[56] J. Liqiang, Q. Yichun, W. Baiqi, L. Shudan, J. Baojiang, Y. Libin, F. Wei, F. Honggang, S. Jiazhong, Review of photoluminescence performance of nano-sized semiconductor materials and its relationships with photocatalytic activity, Sol. Energy Mater. Sol. Cells 90 (2006) 1773–1787, https://doi.org/10.1016/j.solmat.2005.11.007.

[57] J.J. Vijaya, G. Sekaran, M. Bououdina, Effect of Cu^{2+} doping on structural, morphological, optical and magnetic properties of MnFe$_2$O$_4$ particles/sheets/flakes-like nanostructures, Ceram. Int. 41 (2015) 15–26, https://doi.org/10.1016/j.ceramint.2013.10.145.

[58] H. Li, T. Hu, N. Du, R. Zhang, J. Liu, W. Hou, Wavelength-dependent differences in photocatalytic performance between BiOBr nanosheets with dominant exposed (0 0 1) and (0 1 0) facets, Appl. Catal. B: Environ. 187 (2016) 342–349, https://doi.org/10.1016/j.apcatb.2016.01.053.

[59] L. Ye, X. Jin, C. Liu, C. Ding, H. Xie, K.H. Chu, P.K. Wong, Thickness-ultrathin and bismuth-rich strategies for BiOBr to enhance photoreduction of CO$_2$ into solar fuels, Appl. Catal. B: Environ. 187 (2016) 281–290, https://doi.org/10.1016/j.apcatb.2016.01.044.

[60] R. Bechara, A. Aboukaïs, J.-P. Bonnelle, X-ray photoelectron spectroscopic study of a Cu–Al–O catalyst under H$_2$ or CO atmospheres, J. Chem. Soc. Faraday Trans. 89 (1993) 1257–1262, https://doi.org/10.1039/FT9938901257.

[61] D. Hill, H. Meyer III, J. Weaver, C. Gallo, K. Goretta, Cu adatom interactions with single-and polycrystalline Bi$_2$Ca$_{1+x}$Sr$_{2-x}$Cu$_2$O$_{8+y}$ and YBa$_2$Cu$_3$O$_{7-x}$, Phys. Rev. B 38 (1988) 11331, https://doi.org/10.1103/PhysRevB.38.11331.

[62] H. Freundlich, Über die adsorption in lösungen, Z. Phys. Chem. 57 (1907) 385–470, https://doi.org/10.1515/zpch-1907-5723.

[63] A. Emeline, G. Kuzmin, D. Purevdorj, V. Ryabchuk, N. Serpone, Spectral dependencies of the quantum yield of photochemical processes on the surface of wide band gap solids. 3. Gas/solid systems, J. Phys. Chem. B 104 (2000) 2989–2999, https://doi.org/10.1021/jp9926589.

[64] X. Gong, W.Y. Teoh, Modulating charge transport in semiconductor photocatalysts by spatial deposition of reduced graphene oxide and platinum, J. Catal. 332 (2015) 101–111, https://doi.org/10.1016/j.jcat.2015.08.028.

[65] J. Sýkora, Photochemistry of copper complexes and their environmental aspects, Coord. Chem. Rev. 159 (1997) 95–108, https://doi.org/10.1016/S0010-8545(96)01299-4.

[66] X. Lv, I. Rodriguez, C. Hu, J. Shang, P.-H.-L. Sit, C. Ye, G. Oskam, W.Y. Teoh, Modulated anodization synthesis of Sn-doped iron oxide with enhanced solar water splitting performance, Mater. Today Chem. 12 (2019) 7–15, https://doi.org/10.1016/j.mtchem.2018.11.012.

[67] C.-P. Hsu, K.-M. Lee, J.-T.-W. Huang, C.-Y. Lin, C.-H. Lee, L.-P. Wang, S.-Y. Tsai, K.-C. Ho, EIS analysis on low temperature fabrication of TiO₂ porous films for dye-sensitized solar cells, Electrochim. Acta 53 (2008) 7514–7522, https://doi.org/10.1016/j.electacta.2008.01.104.

[68] M. Chen, W. Chu, Photocatalytic degradation and decomposition mechanism of fluoroquinolones norfloxacin over bismuth tungstate: experiment and mathematic model, Appl. Catal. B: Environ. 168 (2015) 175–182, https://doi.org/10.1016/j.apcatb.2014.12.023.

[69] Y. Li, J. Niu, W. Wang, Photolysis of enrofloxacin in aqueous systems under simulated sunlight irradiation: kinetics, mechanism and toxicity of photolysis products, Chemosphere 85 (2011) 892–897, https://doi.org/10.1016/j.chemosphere.2011.07.008.

[70] S. Jiao, S. Zheng, D. Yin, L. Wang, L. Chen, Aqueous photolysis of tetracycline and toxicity of photolytic products to luminescent bacteria, Chemosphere 73 (2008) 377–382, https://doi.org/10.1016/j.chemosphere.2008.05.042.

[71] C. Guo, S. Gao, J. Lv, S. Hou, Y. Zhang, J. Xu, Assessing the photocatalytic transformation of norfloxacin by BiOBr/iron oxides hybrid photocatalyst: kinetics, intermediates, and influencing factors, Appl. Catal. B: Environ. 205 (2017) 68–77, https://doi.org/10.1016/j.apcatb.2016.12.032.

[72] P. Makoś, A. Przyjazny, G. Boczkaj, Methods of assaying volatile oxygenated organic compounds in effluent samples by gas chromatography—a review, J. Chromatogr. A 1592 (2019) 143–160, https://doi.org/10.1016/j.chroma.2019.01.045.

[73] Y. Nosaka, M. Kishimoto, J. Nishino, Factors governing the initial process of TiO₂ photocatalysis studied by means of in-situ electron spin resonance measurements, J. Phys. Chem. B 102 (1998) 10279–10283, https://doi.org/10.1021/jp982886n.

[74] Y. Chen, S. Yang, K. Wang, L. Lou, Role of primary active species and TiO₂ surface characteristic in UV-illuminated photodegradation of Acid Orange 7, J. Photochem. Photobiol. A: Chem. 172 (2005) 47–54, https://doi.org/10.1016/j.jphotochem.2004.11.006.

[75] M. Yin, Z. Li, J. Kou, Z. Zou, Mechanism investigation of visible light-induced degradation in a heterogeneous TiO₂/Eosin Y/Rhodamine B system, Environ. Sci. Technol. 43 (2009) 8361–8366, https://doi.org/10.1021/es902011h.